Monthly Notices
of the
ROYAL ASTRONOMICAL SOCIETY

MNRAS **492,** 993–1007 (2020)
Advance Access publication 2019 December 17

doi:10.1093/mnras/stz3524

Structural analysis of disc super star clusters of M82: size and profile shape at intermediate ages

B. Cuevas-Otahola ,★ Y. D. Mayya ,★ I. Puerari and D. Rosa-González

Instituto Nacional de Astrofísica, Óptica y Electrónica, 72840 Puebla, Mexico

Accepted 2019 December 12. Received 2019 December 11; in original form 2019 November 2

ABSTRACT

We present the structural parameters of 99 super star clusters (SSCs) in the disc of M82. Moffat-EFF, King, and Wilson models were fitted using a χ^2-minimization method to background-subtracted surface brightness profiles in the *F435W* (*B*), *F555W* (*V*), and *F814W* (*I*) bands of the Advanced Camera for Surveys (ACS) of the *Hubble Space Telescope*. The majority of the SSC profiles are best fitted by the Moffat-EFF profile. The scale parameter $r_{\rm d}$ and the shape parameter γ in the three filters are identical within the measurement errors. The analysed sample is big enough to allow the characterization of the distributions of core radii $R_{\rm c}$ and γ. The obtained distribution of $R_{\rm c}$ follows a lognormal form, with centre and $\sigma\log\left(\frac{R_{\rm c}}{pc}\right)$ being 1.73 pc and 0.25, respectively. The γ distribution is also lognormal with centre and $\sigma\log(\gamma)$ being 2.88 and 0.08, respectively. M82 is well known for the absence of current star formation in its disc, with all disc SSCs older than 50 Myr and hardly any cluster older than ∼300 Myr. The derived distributions compare very well with the distributions for intermediate-age clusters in the Large Magellanic Cloud (LMC), which is also a low-mass late-type galaxy similar to M82. On the other hand, the distributions of $R_{\rm c}$ in both these galaxies are shifted towards larger values as compared to SSCs of similar age in the giant spiral galaxy M83. M82 and LMC also span a narrower range of γ values as compared to that in M83.

Key words: catalogues – (Galaxy:) globular clusters: general – galaxies: clusters: general.

1 INTRODUCTION

Understanding the formation and evolution of globular clusters (GCs) has been an active field of research in astrophysics over the last half century (Forbes et al. 2018). The discovery of clusters as dense ($\rho \gtrsim 10^3\,{\rm M}_\odot/pc^3$) and massive ($10^4$–$10^6\,{\rm M}_\odot$) as GCs, but relatively young, known as young massive clusters (YMCs) or super star clusters (SSCs), has given a new impetus to these studies in the last two decades (Bastian 2016). SSCs are often thought to be the progenitors of GCs, and hence their study has the potential to throw light on the processes that the GCs may have experienced during their early evolution (Portegies Zwart, McMillan & Gieles 2010). SSCs are subjected to different physical processes at different time-scales: At short ($\lesssim 10^7$ yr) and intermediate time-scales (10^7–10^8 yr), stellar evolutionary processes (stellar winds, supernovae, etc.) play a role; at later times ($\gtrsim 10^8$ yr), dynamical processes start becoming important: the most dominant of them being the gravitational shocks due to the interaction of the cluster with the tidal field of its host galaxy, and two-body relaxation (Spitzer 1987). These processes increase the velocity of some stars above the escape velocity, forcing them to leave the cluster, resulting in the dissipation and/or complete disruption of the cluster. The selective loss of high-velocity stars from the central regions of the clusters leads to collapse of the core at late times (Lynden-Bell, Wood & Royal 1968). The extent to which a cluster is subjected to these effects depends on its three-dimensional location in its host galaxy, galactocentric distance, in addition to the gravitational potential field of the host galaxy itself (Fall & Zhang 2001). Besides, clusters located in the disc suffer from encounters with Giant Molecular Clouds when they pass through the spiral arms (Gieles et al. 2006). Mackey et al. (2008) analysed the effect of binary and single black holes and found them to be responsible for the expansion of the core at times $\gtrsim$600 Myr in clusters in the Large Magellanic Clouds (LMC). In the presence of a tidal field, the sizes of the expanding clusters would be limited to their tidal radius (Gieles 2013).

The structure of star clusters has been modelled theoretically using autogravitating isothermal spheres of lowered kinetic energy in the presence of external tidal forces. These configurations, usually known as King models following the classical treatment of King (1966), explain satisfactorily the observed surface brightness profiles (SBPs) of old stellar systems such as GCs (Baumgardt & Hilker 2018). The most salient feature of these SBPs is the existence of a core-halo structure, with the core characterized by the core radius and the halo limited by the tidal radius. On the other hand, SBPs of slightly younger systems, such as the blue population of

★ E-mail: bolyumbra@gmail.com (BC-O); ydm@inaoep.mx (YDM)

clusters in the LMC, lack core-halo structure and instead follow power-law forms. Elson, Fall & Freeman (1987) found that these SBPs are well represented by Moffat profiles (Moffat-EFF profiles, henceforth). The profile of the most massive and luminous SSC in the LMC, R136, is also consistent with a Moffat-EFF profile (Elson et al. 1992). Mackey & Gilmore (2003a) fitted Moffat-EFF profiles to the SBPs of 53 star clusters in the LMC to obtain their structural parameters. Wilson profiles, originally proposed by Wilson (1975) to characterize SBPs of elliptical galaxies, are also found to be good fits to the SBPs of SSCs in the LMC (McLaughlin & van der Marel 2005). The power-law nature of SBPs at relatively younger ages is understood to be due to the contribution of stars in the unbound halo (Elson, Fall & Freeman 1987; Moreno, Pichardo & Velázquez 2014).

The *Hubble Space Telescope* (*HST*), especially the wide field of the Advanced Camera for Surveys (ACS), has enabled the detection of large populations of SSCs in external galaxies, some examples being M82 (O'Connell et al. 1995; Melo et al. 2005; Mayya et al. 2008), M51 (Chandar et al. 2011), M81 (Chandar, Ford & Tsvetanov 2001; Santiago-Cortés, Mayya & Rosa-González 2010), M83 (Bastian et al. 2011; Ryon et al. 2015), and Antennae (NGC4038/4039) (Whitmore & Schweizer 1995). Clusters have been reported in 20 other nearby spiral and irregular galaxies using the Hubble Legacy Archive data (Whitmore et al. 2016).

Modern χ^2-minimization technique allows the analysis of the SBPs of SSCs with empirical formulae in an objective way. Moffat-EFF and empirical formulae for King models (King 1962), available directly in profile analysing tools such as ISHAPE (Larsen 1999) and GALFIT (Peng et al. 2010), are the most often used profiles for fitting SBPs of SSCs. The output parameters commonly obtained by such an analysis are core radius and half-light radius, often for an assumed form of the profile shape (e.g. Bastian et al. 2008). Ryon et al. (2015, 2017) carried out the analysis of structural parameters on the *HST* images of ∼700 YMCs in the giant spiral M83, and in two late-type galaxies (NGC 628 and NGC 1313). They obtained core radius, half-light radius, and the shape parameters using Moffat-EFF profile in GALFIT for 478 YMCs that are well resolved on the *HST* images. For the rest of the YMCs, they obtained half-light radius based on an empirical relation between the concentration index, defined as the difference in magnitudes between 1 and 3 pixel radius apertures, and half-light radius on mock YMCs. YMCs they analysed are in general younger than 1 Gyr, and constitute the largest sample of intermediate-age YMCs with uniformly determined structural parameters.

McLaughlin & van der Marel (2005) proposed an alternative technique to obtain structural parameters of star clusters. Their method involves fitting the observed profiles directly with the profiles generated using dynamical models that have underlying physical basis such as King (1966) and Wilson (1975). They also suggested using Jeans theorem to construct dynamical models that are consistent with the empirical Moffat-EFF profile. They used this technique to obtain a complete set of dynamical parameters, not just core radius and half-light radius, for GCs in the Milky Way and Fornax galaxies, and blue and red star clusters in the SMC and LMC galaxies. The technique has been recently extended by Sollima et al. (2015) to implement anisotropic King–Michie models. For clusters of known age, and hence known photometric masses, this technique is able to extract the central and line-of-sight velocity dispersions. The latter parameter could be determined observationally using high-spectral resolution observations, which allows a direct verification of the validity of the assumption of the dynamical models used. The *HST* images of galaxies that are nearer than ∼5 Mpc have sufficient spatial resolution (1 pix = 1.25 pc at 5 Mpc) for the construction of SBPs good enough not only for the determination of their sizes, but also for a detailed analysis using dynamical models. Beyond the Milky Way, M31 and NGC5128 are the only two giant galaxies where SSC profiles have been analysed using dynamical models (Barmby et al. 2007; McLaughlin et al. 2008; Wang & Ma 2013).

M82 is an excellent candidate to carry out such a study, as it is relatively nearby (3.63 Mpc; Freedman et al. 1994), and has a rich population of clusters in its nucleus and disc (Mayya et al. 2008). Spectroscopic ages have been obtained for around 40 of the disc SSCs. The derived ages occupy a relatively narrow range between 50 and 300 Myr (Konstantopoulos et al. 2009). Mayya et al. (2006) suggested, based on the analysis of the photometric, dynamical, and chemical properties, that the entire galaxy participated in a disc-wide burst of duration of a few hundred million years. The disc stopped forming stars around 50 Myr ago, which is well supported by the absence of red supergiants in its disc (Davidge 2008). The disc-wide burst and the formation of disc clusters were most likely triggered by the interaction of M82 with its neighbours M 81 and NGC 3077 (Yun 1999). The narrow age range of disc SSCs is consistent with them being formed in the disc-wide burst. The existence of a few hundreds of massive SSCs, all of ages intermediate between the YMCs and the old GCs, gives us a great opportunity to understand the dynamical effects experienced by evolving clusters.

In Section 2, we summarize the general properties of the sample of SSCs in the disc of M82, as well as the procedure followed in this work to obtain the background-subtracted SBPs. In Section 3, we describe the SBPs expected in theoretical models such as King and Wilson, and empirical formulae (Moffat-EFF), as well as the procedure followed to obtain the structural parameters from the observed SBPs. Model-derived parameters are presented and their statistical properties discussed in Section 4. The results are summarized in Section 5.

2 M82 SSC SAMPLE AND EXTRACTION OF SURFACE BRIGHTNESS PROFILES

The sample of SSCs for structural analysis was selected from the catalogue of M82 disc SSCs from Mayya et al. (2008), which consists of 393 objects, and is based on the detection of SSCs in the *F435W* (*B*), *F555W* (*V*), and *F814W* (*I*) bands of the *HST*/ACS. The entire sample is presented in table 3 of Mayya et al. (2008). In Section 2.2, we will compare the magnitude and colour properties of the subsample with respect to the entire sample.

2.1 SBPs

We used the same images that were used for cluster detection to extract SBPs. These images were part of the *HST* Legacy Survey, which were made available in reduced form by the Hubble Heritage Team (Mutchler et al. 2007). The image scale corresponds to 0.05 arcsec pixel^{-1} and covers the entire optical extent of M82. Exposure times were 1600, 1360, and 1360 s in filters *B*, *V*, and *I*, respectively. The zero-point magnitudes in the Vega system were extracted from Sirianni et al. (2005), with values 25.779, 25.724, and 25.501 for the *B*, *V*, and *I* bands, respectively.

Profile-fitting packages such as GALFIT and ISHAPE analyse two-dimensional (2D) images to obtain structural parameters of star clusters. On the other hand, azimuthally averaged one-dimensional

(1D) profiles have been used traditionally to obtain structural parameters of well-resolved clusters in the Milky Way and Local Group galaxies (e.g. Elson et al. 1987; McLaughlin & van der Marel 2005). The profile functions used in both these techniques are 1D profiles applicable to spherically symmetric 3D models. Moreover, derived structural parameters such as core radius and half-light radius refer to the radially symmetric configurations. We hence adopt the 1D technique in this study. The *ellipse* task (Jedrzejewski 1987) in IRAF/STSDAS package is the standard tool to obtain the azimuthally averaged 1D profiles of extended objects. Though the task is developed for analysing the SBPs of external galaxies, the task does an excellent job in obtaining 1D SBPs of clusters on the *HST* images. We fixed the centres of the ellipses at the centroids of the SSCs, and obtained the SBPs at successive *HST*/ACS pixels, with a width of 1 pixel (0.88 pc at the distance of M82). The task also calculates the azimuthal dispersions in the intensity at each radial bin, which is a measure of errors in the SBPs. We left the ellipticity ($\epsilon = 1 - b/a$, where a and b are semimajor and semiminor axes, respectively) and position angle as free parameters in a first run of the task. The distribution of ellipticities peaks at 0.19 with only 25 per cent of the SSCs having higher ellipticities. This is illustrated in Fig. A1 of the Appendix and Tab. A1. Thus, the majority of the SSCs are nearly circular. With $\epsilon = 0.3$, the well-known SSC M82-F (D1) is one of the most elongated clusters. The SBPs obtained for this cluster using circular and elliptical ($\epsilon = 0.30$) apertures are similar (see Fig. A2 in the Appendix). Smith & Gallagher (2001) also found that the half-light radii obtained from profiles using circular and elliptical apertures for M82-F are similar, which confirms that the derived structural parameters are not very sensitive to small differences in ellipticities. We hence fixed the ellipticity at the minimum value permitted by the task, which is $\epsilon = 0.05$.

The SBPs obtained by the *ellipse* task contain background contribution, which should be subtracted in order to obtain pure cluster profiles. This background in the case of M82 clusters mainly comes from its disc, which varies appreciably from one cluster to another. This makes the measurement of background for each cluster mandatory. We analysed the four corners of the cut-outs for finding an appropriate local background value for each SSC. Median and standard deviation values were obtained in boxes of 10×10 pixel size at the four corners of the cut-out images, the minimum of these four values being chosen as the background $I_{\rm bg}$ and the noise $\sigma_{\rm bg}$, respectively. For each background-subtracted profile, we determined a limiting radius, defined as the outermost point of the profile at which the cluster surface brightness is equal to 3 times $\sigma_{\rm bg}$. We refer to this radius as $R_{3\sigma}$.

Cluster SBPs are expected to monotonically decrease up to $R_{3\sigma}$. However, we found that the majority of the profiles have an inflexion point at $R < R_{3\sigma}$. Visual examination of the images suggested that this is due to stars or clusters in the neighbourhood of the object of analysis. When possible, we masked the contaminating sources in each cut-out image before obtaining SBPs. In a few cases, the masks were successful in producing SBPs free from contamination from neighbours. However, in the majority of the cases, SBPs are affected due to some residual contribution from the neighbours. This is because in most of the cases the contaminating source is another SSC, which occupies a non-negligible number of pixels of the cut-out image. We took into account this effect by defining a fitting radius for each SSC, within which the profile is free from contamination from a neighbour. We obtained this radius by determining the innermost inflexion point $R_{\rm ip}$, such that at $R_{\rm ip}$, $\frac{d^2I}{{\rm d}R^2} = 0$, for each background-subtracted profile. In general, the fitting radius, $R_{\rm fit}$, is the minimum of $R_{\rm ip}$ and $R_{3\sigma}$. However, in all cases, $R_{\rm ip} < R_{3\sigma}$, and hence, $R_{\rm fit} = R_{\rm ip}$.

The profile analysis was carried out in the *BVI HST*/ACS bands. In each of these bands, the above procedure is repeated. Hence, we have a set of $I_{\rm bg}$, $\sigma_{\rm bg}$, $R_{\rm ip}$, $R_{3\sigma}$, and $R_{\rm fit}$ for each band.

In Fig. 1, we illustrate the procedure adopted for obtaining the fitting radius for two clusters, one unaffected by a contaminating object (D8) and the other with a bright nearby contaminating source (D4). In the former case, $R_{\rm ip}$ is almost equal to $R_{3\sigma}$, whereas in the latter case, $R_{\rm ip}$ is less than half of $R_{3\sigma}$. The bump immediately beyond $R_{\rm ip}$ is due to the contaminating object, which can be seen in the RGB image. In Table 1, we give the values of $R_{\rm fit}$, $R_{3\sigma}$, and the background surface brightness (μ) and its error ($\delta\mu$), as well as the R.A. and DEC for all SSCs. The error is calculated as $\delta\mu = 1.086\left(\frac{\sigma_{\rm bg}}{I_{\rm bg}}\right)$. $R_{\rm fit}$ in all cases is the inflexion radius $R_{\rm ip}$.

In the following section, we will discuss the global properties of the selected 99 SSCs with respect to the total SSCs disc sample.

2.2 Selection and characteristics of the disc subsample

In order to obtain reliable structural parameters from the *HST* images, star clusters have to satisfy certain criteria. The most important of these criteria is that they have enough number of pixels for profile analysis. In the absence of a contaminating source, the number of pixels for analysis depends on the intrinsic size of the cluster. Another criterion for the selection of clusters is that the extracted profile is well fitted by one of our models, quantified by χ^2 statistics, and described in the next section. We carried out an analysis of synthetic clusters in order to define the $R_{\rm fit}$ necessary to reliably recover the input parameters, which is also described in the next section. Based on this analysis, we considered a cluster to be good for analysis (1) if the $R_{\rm fit} \geq 8$ pixels in at least two bands and (2) the χ^2 of the best fit is less than $3\times\ \nu$, where ν is the number of degrees of freedom (Avni 1976; Wall & Jenkins 2003) (criteria 1 and 2, respectively). In the majority of the cases, the B and V bands have similar behaviour with the I band displaying a different behaviour, with ∼16 per cent having less than 8 pixels in I. The imposition of this criterion reduced our sample size to a subsample of 99 SSCs.

In order to determine how representative is the subsample with respect to the total sample, we compare the distributions of three of the most important characteristics for the two samples in Fig. 2. The chosen characteristics are: V magnitude, $B - V$ colour, and the photometric mass. Given that most of the disc SSCs are formed in a disc-wide burst around 300 Myr ago, little dispersion is expected in the intrinsic colours and mass-to-light ratios of the SSCs. However, M82 SSCs suffer from considerable extinction, which gives rise to large dispersion in their colours. In this work, we assume that the entire dispersion in the colour histogram is caused by reddening. Hence, extinction-corrected magnitude is directly a measure of the mass for these SSCs. Our subsample contains between 20 and 40 per cent of the total sample for $B - V = 0.2$–2.0 mag, $V = 18$–22 mag, and $\log M/{\rm M}_\odot = 4.5$–$6.5$ dex. In summary, our subsample represents the bright ($V > 18.0$ mag), massive ($M > 3 \times 10^4\,{\rm M}_\odot$) end of the total sample of SSCs, covering uniformly the entire range of extinction values. This subsample is complete above mass of $M > 3 \times 10^4\ {\rm M}_\odot$, which is very close to the turnover in the mass function for the entire cluster sample (Mayya et al. 2008). Thus, our subsample is representative of the massive end of the luminosity function.

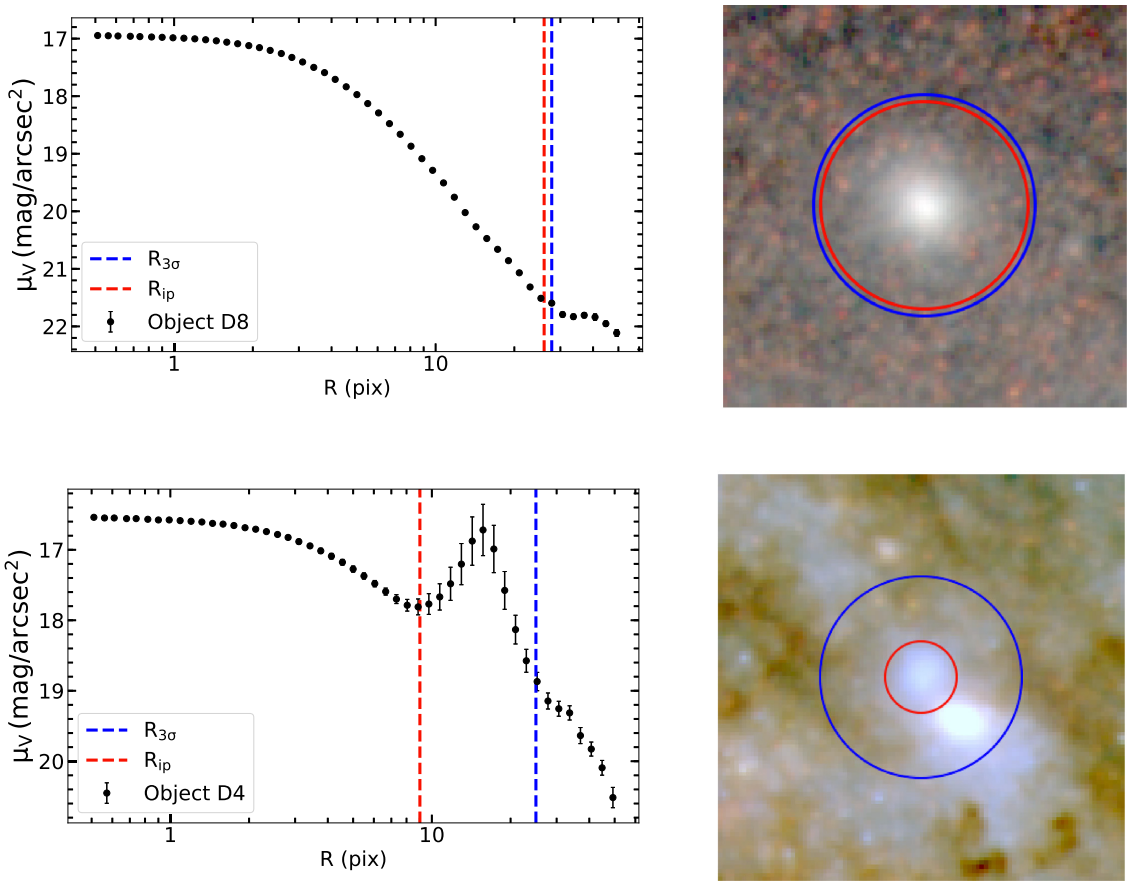

Figure 1. The *V*-band SBPs (left) and RGB image, constructed from the *I* (R), *V* (G), and *B* (B) bands (right) of two clusters, illustrating the procedure adopted for selecting the fitting radius. In the top, we illustrate it for the SSC D8, an isolated cluster, whereas in the bottom, we illustrate it for a highly contaminated, but still useful, SSC D4. The $R_{3\sigma}$, the radius where the background-subtracted intensity is $3 \times \sigma_{\rm bg}$, and $R_{\rm ip}$, the inflexion radius where $\frac{d^2I}{dR^2} = 0$, are shown by vertical dashed lines (left) and circles (right) of blue and red colours, respectively. Note that the profiles are shown with logarithmic steps to illustrate the inner and outer profile shapes, simultaneously.

Table 1. Fitting radius and background value for all M82 disc SSCs.

ID[a]	R.A. (deg)	DEC (deg)	$R_{\rm ip}$ (pix)	$R_{3\sigma}$ (pix)	$\mu_{\rm bg} \pm \delta\mu$ (mag arcsec^{-2})
(1)	(2)	(3)	(4)	(5)	(6)
D1	148.946 15	69.678 42	19	23	18.42 ± 0.22
D2	149.003 84	69.685 13	14	24	18.20 ± 0.30
D3	149.014 20	69.686 72	18	50	18.89 ± 0.44
D4	148.946 55	69.678 56	9	26	18.48 ± 0.22
D5	148.944 80	69.677 37	11	16	19.11 ± 0.32
D6	149.009 52	69.685 84	18	34	18.74 ± 0.32
D7	149.003 72	69.685 66	11	14	17.84 ± 0.17
D8	149.059 42	69.699 09	25	26	20.34 ± 0.12
D9	148.981 91	69.684 97	14	34	19.02 ± 0.21
D10	148.987 67	69.685 37	9	28	18.88 ± 0.16

Note. [a]IDs from Mayya et al. (2008). The 'D' preceding the numbers stands for 'disc' sample.

3 DETERMINATION OF STRUCTURAL PARAMETERS

Structural parameters were obtained by fitting the observed SBPs with PSF-convolved theoretical profiles. The fitted model profiles are Moffat-EFF (Elson et al. 1987), King (King 1966), and Wilson (Wilson 1975). We followed the procedure described in detail in McLaughlin & van der Marel (2005), which we summarize briefly in this section.

3.1 Dynamical models of star clusters

King and Wilson models are based on a 'lowered' Maxwellian kinetic energy distribution function of stars. These two model structures differ only in the outer halo regions, which is due to an extra term in the Wilson formulation, and are defined in terms of the distribution function of a relative energy $\mathcal{E} = -E + \Phi_0$, where E is the total energy for a star moving with an isotropic velocity v under a potential Φ. The term Φ_0 is a constant such that the relative

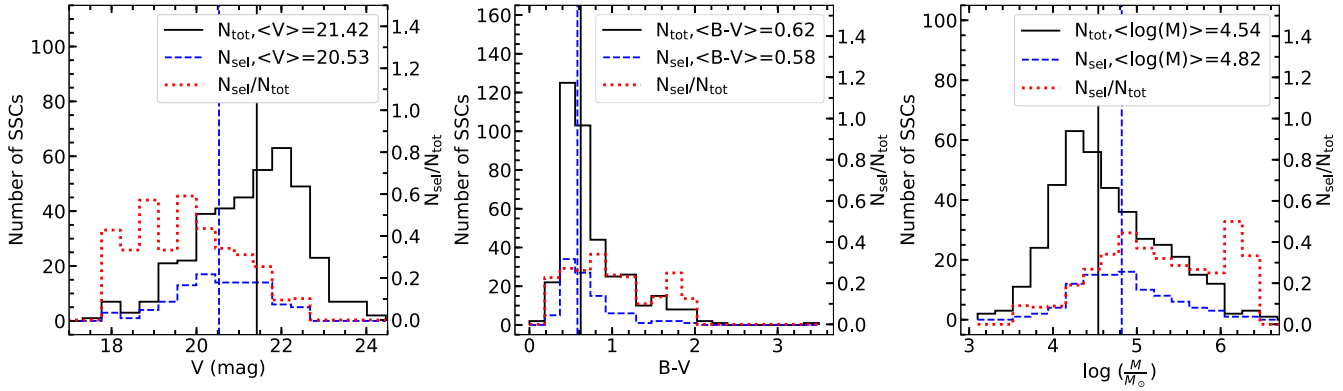

Figure 2. Comparison of distributions of V magnitude (left), $B-V$ (middle), and cluster mass (right) of all M82 disc SSCs (black solid line) with the selected sample (99 clusters) (blue dashed line). Median values of the distributions are shown by the vertical lines and written in the top-right corner. The fraction of objects ($N_{\rm sel}/N_{\rm tot}$) in each bin is shown by a red dotted line.

energy is positive everywhere in the cluster. Under this formulation, the relative potential $\Psi = -\Phi + \Phi_0$ and $\mathcal{E} = \Psi - \frac{1}{2}v^2$. The models described above are given by

$$\text{King}: f(\mathcal{E}) \propto \begin{cases} e^{(\mathcal{E}/\sigma_0^2)} - 1, & \mathcal{E} > 0, \\ 0, & \mathcal{E} \leqslant 0, \end{cases}, \tag{1}$$

$$\text{Wilson}: f(\mathcal{E}) \propto \begin{cases} e^{(\mathcal{E}/\sigma_0^2)} - 1 - \frac{\mathcal{E}}{\sigma_0^2}, & \mathcal{E} > 0, \\ 0, & \mathcal{E} \leqslant 0, \end{cases}, \tag{2}$$

where σ_0 is a scale parameter that measures the core dispersion velocity defined as

$$\sigma_0^2 \equiv \frac{4\pi G \rho_0 r_0^2}{9}, \tag{3}$$

where ρ_0 is the central stellar density and r_0 is the scale radius, commonly referred to as King radius. These models are parametrized by a dimensionless potential $W = \Psi/\sigma_0^2$, which is defined at all radii inside the tidal radius $r_{\rm t}$, and has the boundary values of $W(r=0) \equiv W_0$ and $W(r=r_{\rm t}) = 0$. W_0 is a measure of the central potential, being directly related to the often-used concentration parameter $c = \log(\frac{r_{\rm t}}{r_0})$. In this work, we varied the W_0 values between 2 and 15, which corresponds to $c = 0.5$ and 3.3 for King models and $c = 0.7$ and 4.1 for Wilson models.

The solution of these equations is expressed as a function of $W(r)$, which is directly related to the 3D density function, $\rho(r)$ through the Poisson equation (as well as a normalized velocity dispersion profile, in terms of the central velocity dispersion, solving Jeans equation). The observable quantity $I(R)$ is obtained from $\rho(r)$ by projecting it into the plane of the sky along the R axis following the standard formulation [e.g. equation (2.138)a in Binney & Tremaine 1987] and dividing by the mass-to-light ratio Γ:

$$I(R) = \frac{\Sigma(R)}{\Gamma} = \frac{2}{\Gamma}\int_R^{R_{\rm t}} \frac{\rho(r)}{(r^2 - R^2)^{\frac{1}{2}}} r\,{\rm d}r, \tag{4}$$

where the integration limits are defined as $R = r/r_0$ and $R_{\rm t} = r_{\rm t}/r_0$, r_0 being obtained by fitting model profiles to observed SBPs. The cluster extends up to the tidal radius $r_{\rm t}$, where by definition $E = 0$.

The Moffat-EFF profiles were proposed by Elson et al. (1987) as a convenient modification of the empirical King profile (King 1962) to fit the SBPs of LMC clusters. The functional form of the profile is

$$I(R) = \frac{(\gamma - 2)L_{\rm tot}}{2\pi r_{\rm d}^2}\left[1 + \left(\frac{R}{r_{\rm d}}\right)^2\right]^{-\gamma/2}, \tag{5}$$

where R is the semimajor axis of the observed profile, and $r_{\rm d}$ is the characteristic radius, which is related to the core radius $R_{\rm c}$ by

$$r_{\rm d} = \frac{R_{\rm c}}{(2^{2/\gamma} - 1)^{1/2}}. \tag{6}$$

Once γ and $r_{\rm d}$ are determined from the fitting, the 3D luminosity density profile can be calculated using the expression

$$j(r) = j_0\left(1 + \frac{r^2}{r_{\rm d}^2}\right)^{-(\gamma+1)/2}. \tag{7}$$

The mass density is obtained using $\rho(r) = \Gamma j(r)$. On the other hand, a velocity profile is found solving Poisson and Spherical Jeans equations, giving rise to a normalized velocity dispersion profile in terms of the central velocity dispersion σ_0. The surface mass density Σ is found by projecting the volume mass density $\rho(r)$ into the plane of the sky, following equation (4). The surface density profile also allows us to calculate numerically $R_{\rm h}$, the radius containing half the total light.

3.2 PSFs

Intrinsic cluster profiles are broadened due to the PSF of the instrument, and hence in order to determine the structural parameters, especially the core parameter, it is essential to convolve the model profiles with the instrumental PSF profiles before comparing with observed SBPs. We used the PSFex (Bertin 2011) tool to obtain a PSF in each of the three bands. Before using this tool, we selected a list of suitable stars in each of these bands using SEXTRACTOR (Bertin & Arnouts 1996). A star is considered to be suitable for PSF construction if it is isolated, and bright, but not saturated. We used various SEXTRACTOR output parameters to select these PSF stars. More than 1000 stars were used in each of the bands for this purpose (1234 in B, 1401 in V, and 1328 in I). The resulting PSFs are shown in Fig. 3.

In order to illustrate that our selected SSCs are easily distinguishable from stars, we compare in Fig. 4 the profile for one of the smallest SSCs with that of the PSF. Each displayed profile is an azimuthally averaged profile obtained as described in Section 2.1. In this illustration, both profiles are sampled in logarithmic steps successively increasing by 10 per cent. Profiles generated for fitting purposes have linear steps of 1 pixel size for clusters and 0.5 pixel size for the PSF.

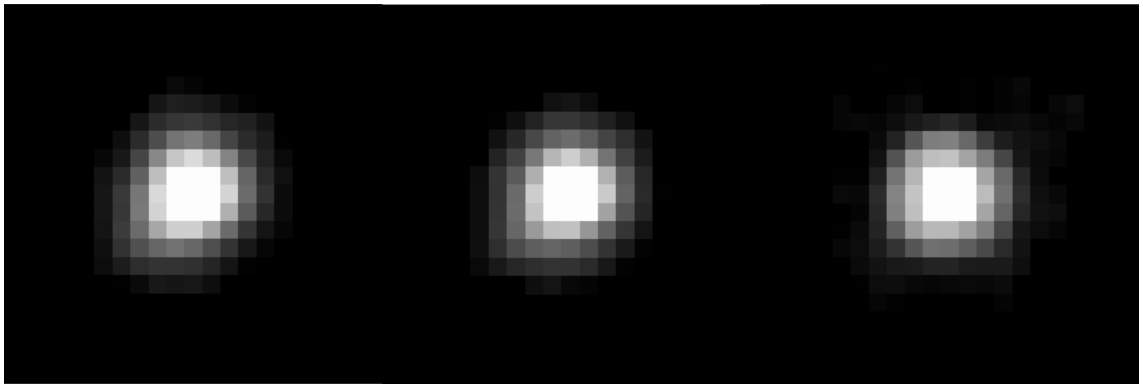

Figure 3. PSF images in the *B* (left), *V* (middle), and *I* (right) bands calculated using PSFex (Bertin 2011).

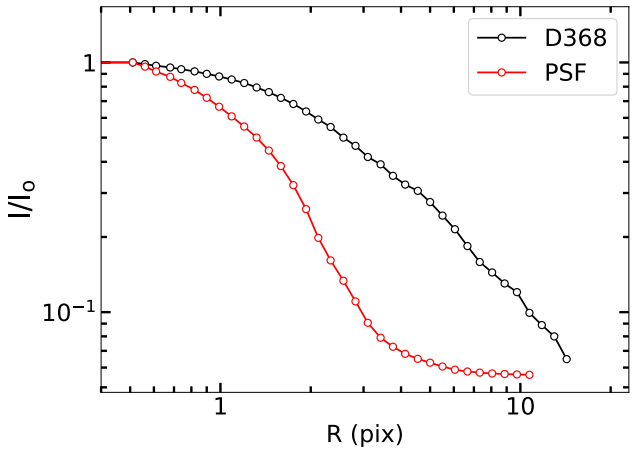

Figure 4. PSF profile (red) compared to that for one of the most compact clusters of the sample (D368: black), both normalized to their peak values in the *V* band. These radial profiles are obtained using the IRAF task *ellipse*, at logarithmic steps increasing successively by 10 per cent. The cluster profiles are clearly broader than the PSF profiles.

3.3 χ^2 method and errors on derived parameters

In order to extract structural parameters from SBPs, we used the χ^2-minimization technique. We define χ^2 as

$$\chi^2 = \sum_{i=1}^{N\text{pts}} \frac{(I_{\text{obs}_i} - \tilde{I}_{\text{model}_i})^2}{\sigma_i^2}, \quad (8)$$

where I_{obs_i} and $\tilde{I}_{\text{model}_i}$ are the i-th point in the observed SBP and PSF-convolved model profile, respectively. The summation is over Npts, within the fitting radius, R_{fit}. The σ_i term is the I_{err} of the azimuthally averaged i-th isophote, as calculated by the *ellipse* task.

The convolution of the model with the PSF was performed with the FORTRAN routine CONVLV from NUMERICAL RECIPES (Press et al. 1992), which performs an FFT. For this purpose, we sampled both the PSF and the model at linear steps of 0.5 pixels, which is two times the sampling of the objects.

The χ^2-fitting technique is implemented using a FORTRAN program developed for this purpose. The best-fitting parameters were obtained using a two-step procedure: In the first step, we used a coarse grid in the parameter space to obtain a preliminary minimum χ^2. In the second step, we used 10 times better steps and searched for minimum $\chi^2 \equiv \chi^2_{\text{min}}$ around the preliminary parameters set, to cover a range of 4 times the coarse step. In Table 2, we give the range and the coarse step size for the parameters. The fitting procedure starts with coarse grids. Once a local minimum is found, the fine grid is used. We repeated the second step around the next two local minima of the first step. In all cases, the best-fitting parameter set using fine steps is around the values corresponding to the minimum χ^2. This two-step procedure ensures that the recovered parameters have a numerical precision better than the coarse step. This also resulted in a parameter set of nearly 1000 models that satisfy the condition $\chi^2 - \chi^2_{\text{min}} < 1$.

Table 2. Range and step of parameters values for the three fitted models.

Model (1)	r_{d} or r_0 (2)	γ or W_0 (3)
Moffat-EFF	0.05–10; 0.04	0.1–10; 0.04
King	0.05–10; 0.10	2.0–15; 0.10
Wilson	0.05–10; 0.10	2.0–15; 0.10

Note. Col. (1): Model. Col. (2): Moffat-EFF r_{d} or Dynamical (King or Wilson) r_0 ranges and step size in pixels. Col. (3): Moffat-EFF γ parameter or Wilson or King W_0 parameter range and step size.

The errors on the best-fitting parameters for all 99 SSCs were obtained based on the χ^2 statistics. We considered parameter values of all our models for which $\chi^2 - \chi^2_{\text{min}} < 1$, as a set of acceptable values within a 1σ confidence limit. We show this set of parameters in γ versus r_{d} plane as error ellipses for 10 of our objects for the Moffat-EFF profile fits in Fig. 5. The error on r_{d} and γ correspond to the projections of the ellipse along the x-axis and y-axis, respectively. We would like to note that the best-fitting parameters are not necessarily at the centre of the ellipse, implying that the errors on the positive and negative sides are not always the same. A clear tendency is seen for errors being larger for larger values of the parameters. These 1σ confidence limits are reported as the errors on r_{d} and γ for all the clusters in Table 3. A similar analysis was carried out to obtain the errors on the parameters of King and Wilson models, which are also reported in the table.

3.4 Fits on simulated clusters and minimum R_{fit}

As mentioned in Section 2.1, the choice of R_{fit} is crucial in determining reliable structural parameters. With the aim of determining the minimum number of pixels required for this, we carried out a profile-fitting procedure on simulated clusters. The mock sample of clusters constituted 10 clusters, all following Moffat-EFF profiles

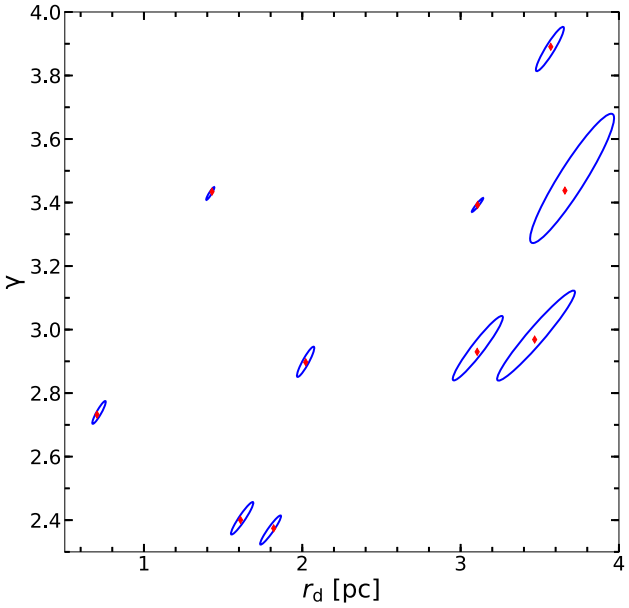

Figure 5. Error ellipses (1σ confidence intervals) of the parameters r_d and γ of models satisfying the criterion $\chi^2 - \chi^2_{min} < 1$ for the brightest 10 observed clusters of the sample. The errors on both axes correspond to the projections of the ellipse along the *x*-axis and *y*-axis. The best-fitting parameters are shown with red diamonds.

and covering the extreme ranges of the parameter space. An rms noise is added to the simulated images, which are also convolved with the PSFs described in Section 3.2 in order to simulate the observational effects. The structural parameters of the mock sample were recovered following the same procedure as that for the sample clusters. For each cluster, we obtained structural parameters for several values of R_{fit}, starting at 6 pixels, and all the way up to $R_{fit} = R_{3\sigma}$.

For each of these R_{fit} values, we obtained the best-fitting parameters as well as their error ellipses. We found that for $R_{fit}<8$ pixels, the χ^2_{min} values in general were greater than $3 \times \nu$ and hence do not satisfy our selection criteria. In Fig. 6, we show the results of the simulations in γ versus r_d plane for three values of R_{fit}: (1) $R_{fit} = R_{3\sigma}$, (2) $R_{fit} = R_{ip}$, and (3) $R_{fit} = 8$ pixels. As expected, $R_{fit} = R_{3\sigma}$ has the least error, with the maximum error being for the $R_{fit} = 8$ pixels. Even in the latter case, the recovered values are in good agreement with respect to the initial values. Thus, we conclude from these simulations that the parameter values recovered with $R_{fit} = 8$ pixels for our observed sample are reliable.

3.5 Method to select the best model

A fit is considered to be good if χ^2_{min} is of the order of the degrees of freedom (ν) (Wall & Jenkins 2003), which in our general case is $\nu = N\text{pts} - 2$. However, in fitting SBPs, it is common to obtain $\chi^2_{min} < \nu$, even when fits are good (McLaughlin & van der Marel 2005). This is because, it is necessary to sample the central parts at steps of at least 1 pixel in order to define the SBPs, which is more than a factor of 2 oversampled with respect to the typical PSF values. This makes the SBP values at successive points not completely independent of each

Table 3. Best-fitting parameters in filter *V* for Moffat-EFF, King, and Wilson models.

ID	*N*pts	Model	χ^2_{min}	W_0 or γ	r_0 or r_d (pc)	μ_0 (mag arcsec^{-2})	log I_0 ($L_\odot$ pc^{-2})
(1)	(2)	(3)	(4)	(5)	(6)	(7)	(8)
D1	19	M	12.69	$2.73^{+0.04}_{-0.03}$	$0.70^{+0.06}_{-0.03}$	$13.55^{+0.11}_{-0.06}$	$5.16^{+0.07}_{-0.04}$
		K	22.92	$8.70^{+0.04}_{-0.05}$	$0.92^{+0.10}_{-0.19}$	$13.55^{+0.15}_{-0.28}$	$5.16^{+0.11}_{-0.20}$
		W	10.04	$8.76^{+0.08}_{-0.01}$	$0.84^{+0.19}_{-0.10}$	$13.55^{+0.29}_{-0.14}$	$5.16^{+0.21}_{-0.10}$
D4	9	M	11.57	$2.97^{+0.15}_{-0.13}$	$3.47^{+0.29}_{-0.27}$	$16.50^{+0.46}_{-0.42}$	$3.98^{+0.33}_{-0.30}$
		K	11.65	$7.86^{+7.14}_{-1.36}$	$3.56^{+0.40}_{-0.10}$	$16.50^{+10.1}_{-1.93}$	$3.98^{+7.15}_{-1.36}$
		W	11.72	$8.95^{+6.05}_{-1.55}$	$3.56^{+0.40}_{-0.10}$	$16.50^{+8.57}_{-2.20}$	$3.98^{+6.06}_{-1.55}$
D7	11	M	1.46	$2.37^{+0.04}_{-0.05}$	$1.82^{+0.05}_{-0.10}$	$16.85^{+0.09}_{-0.15}$	$3.84^{+0.07}_{-0.11}$
		K	18.86	$14.96^{+0.04}_{-2.56}$	$2.52^{+0.19}_{-0.10}$	$16.85^{+0.28}_{-3.62}$	$3.84^{+0.20}_{-2.56}$
		W	19.42	$14.96^{+0.04}_{-1.46}$	$2.52^{+0.19}_{-0.10}$	$16.85^{+0.28}_{-2.06}$	$3.84^{+0.20}_{-1.46}$
D8	25	M	68.86	$3.39^{+0.02}_{-0.02}$	$3.11^{+0.04}_{-0.04}$	$16.90^{+0.07}_{-0.07}$	$3.82^{+0.05}_{-0.05}$
		K	166.94	$6.35^{+0.09}_{-0.09}$	$2.86^{+0.20}_{-0.10}$	$16.90^{+0.31}_{-0.19}$	$3.82^{+0.22}_{-0.13}$
		W	84.65	$6.56^{+0.19}_{-0.10}$	$2.96^{+0.19}_{-0.01}$	$16.90^{+0.38}_{-0.14}$	$3.82^{+0.27}_{-0.10}$
D10	9	M	3.84	$2.40^{+0.06}_{-0.04}$	$1.61^{+0.09}_{-0.07}$	$16.39^{+0.15}_{-0.12}$	$4.02^{+0.11}_{-0.08}$
		K	13.08	$14.96^{+0.04}_{-3.15}$	$2.25^{+0.19}_{-0.10}$	$16.39^{+0.28}_{-4.46}$	$4.02^{+0.20}_{-3.16}$
		W	13.62	$14.96^{+0.04}_{-1.85}$	$2.25^{+0.19}_{-0.10}$	$16.39^{+0.28}_{-2.63}$	$4.02^{+0.20}_{-1.86}$
D14	14	M	19.00	$3.89^{+0.06}_{-0.07}$	$3.57^{+0.09}_{-0.11}$	$17.35^{+0.16}_{-0.18}$	$3.64^{+0.11}_{-0.13}$
		K	29.65	$5.20^{+0.10}_{-0.10}$	$3.21^{+0.10}_{-0.10}$	$17.35^{+0.20}_{-0.20}$	$3.64^{+0.14}_{-0.14}$
		W	22.75	$5.20^{+0.04}_{-0.14}$	$3.39^{+0.10}_{-0.19}$	$17.35^{+0.15}_{-0.33}$	$3.64^{+0.11}_{-0.24}$

Note. Col. (1): Cluster name. Col. (2): Number of points used in the fitting procedure. Col. (3): Fitted model, M (Moffat-EFF), (K) Dynamical King, (W) Wilson. Col. (4): Minimum value of χ^2 obtained for the selected model in Col (3). Col. (5): Shape parameter, W_0 for Wilson and Dynamical King models, and γ for Moffat-EFF. Col. (6): Scale parameter, r_0 for Wilson and King, and r_d for Moffat-EFF. Cols. (7 and 8): Central surface brightness in magnitude and luminosity units, respectively. The full table is shown in the electronic edition; a portion is shown here for guidance.

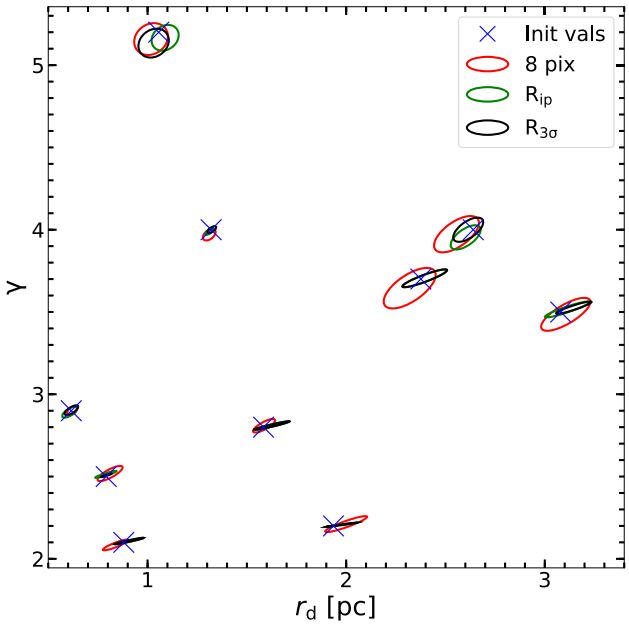

Figure 6. Error ellipses (1σ confidence intervals) of the parameters $r_{\rm d}$ and γ of models satisfying the criterion $\chi^2 - \chi^2_{\rm min} < 1$ for 10 synthetic clusters that mimic the properties of the clusters of the sample. For each synthetic cluster, parameter values for three $R_{\rm fit}$ values are shown: $R_{\rm fit} = 8$ pixels (red), $R_{\rm ip}$ (green), and $R_{3\sigma}$ (black). The initial values are shown by crosses, which are inside the error ellipses even with the $R_{\rm fit} = 8$ pixels.

other, i.e. σ_i of successive points are correlated, making $\chi^2_{\rm min} < \nu$. We used the rms errors in the azimuthally averaged intensities as σ_i in the χ^2 equation, and hence there may be some contribution to the σ_i from real azimuthal variations, which will also make $\chi^2_{\rm min} < \nu$. Some SSCs have $\chi^2_{\rm min} > 3\nu$, which implies that the best-fitting model does not represent perfectly the observed SBP.

In Fig. 7, we show the results for the best-fitting parameters for an illustrative cluster, for each of the three model profiles. In the left-most panel, we show the results for the best-fitting Moffat-EFF model, and in the other two panels, we show the results for the best-fitting Wilson and King models. In the second panel, we show an RGB image for the same cluster. In each panel, fits are shown for the three bands used in this analysis, along with the best-fitting model parameters in each band. The $R_{\rm fit}$ in each band is indicated by vertical lines and $R_{\rm fit}$ for the V band is shown in the RGB image. $R_{\rm fit}$ values in the B and V bands match in general, whereas in the I band, it is generally smaller. The bottom panels show the residual $\Delta\mu = \mu_{\rm obs} - \mu_{\rm model}$.

In most cases, $\chi^2_{\rm min}$ values for the best-fitting Moffat-EFF, King, and Wilson models are not very different, implying that the fits are equally good for more than one model. McLaughlin & van der Marel (2005) proposed a method to determine quantitatively the best among these models. We adopted their technique for fits obtained for each filter for every cluster. This method consists of defining a $\Delta\chi^2$ as

$$\Delta\chi^2 = \frac{\chi^2_{\rm alt} - \chi^2_{\rm ref}}{\chi^2_{\rm alt} + \chi^2_{\rm ref}}, \tag{9}$$

where $\chi^2_{\rm ref}$ and $\chi^2_{\rm alt}$ are the $\chi^2_{\rm min}$ values of the reference model and the model to be compared, respectively. Two models are considered to be equally good if $|\Delta\chi^2| \leq 0.2$, whereas the reference model is good for $\Delta\chi^2 > 0.2$.

In Fig. 8, we show the $\Delta\chi^2$ distributions for all the 99 SSCs with Moffat-EFF as the reference model. Around 45 per cent of the clusters have $|\Delta\chi^2| \leq 0.2$, indicating that all the three models are fitted equally well for these clusters. Moffat-EFF models are good fits for 95–97 per cent of the SSCs, with only 3–5 per cent of SSCs

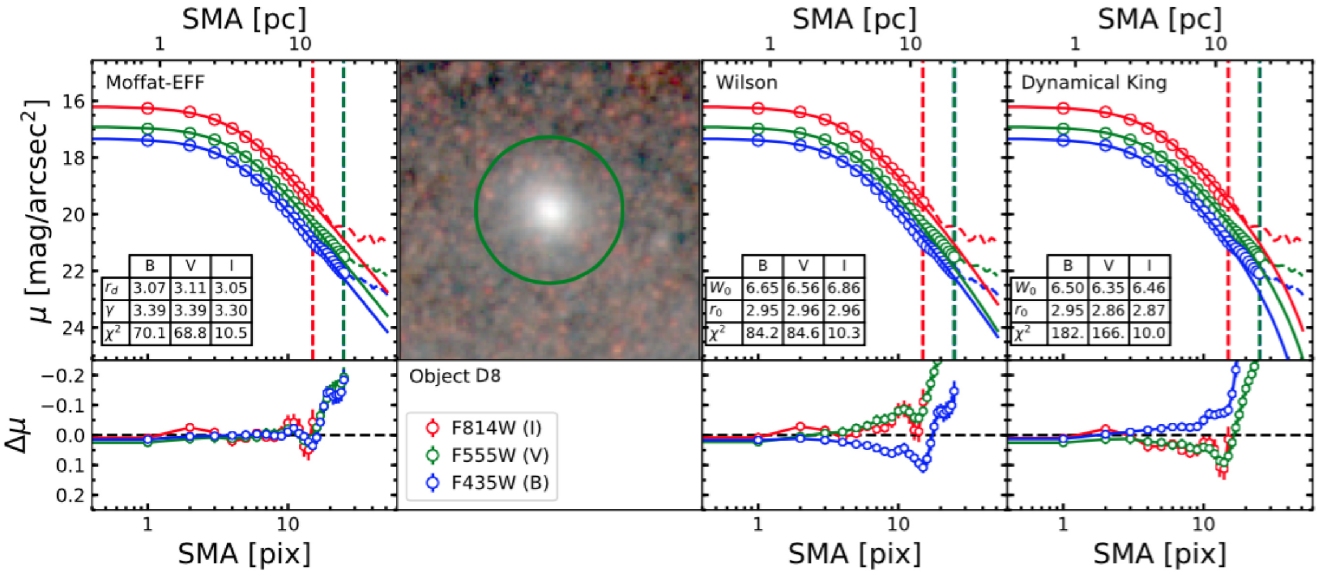

Figure 7. Illustration of the dynamical model fitting of the observed profiles with Moffat-EFF (left most), Wilson (third from left), and Dynamical King (right most). Profiles for SSC D8 in the filters B (blue), V (green), and I (red) are shown, and the fitting radius in the corresponding filter is indicated with dashed vertical lines following the same colour code. In this particular case, the $R_{\rm fit}$ values corresponding to the filters B and V coincide. In the bottom panels, the corresponding residuals ($\Delta\mu = \mu_{\rm obs} - \mu_{\rm model}$) are shown. An RGB cut-out image of the cluster formed using the I(R)-, V(G)-, and B(B)-band images is shown, with a circle indicating the $R_{\rm fit}$ of the V band. Each fitted point is shown by circles for a radius $\leq R_{\rm fit}$, and by dashed lines beyond that. The error bars are shown both in the fittings and the residuals, but are smaller than the symbol size for the great majority of points. The best-fitting parameter values and the $\chi^2_{\rm min}$ for each fit are shown in the embedded tables. The electronic version contains plots such as this for all the 99 SSCs.

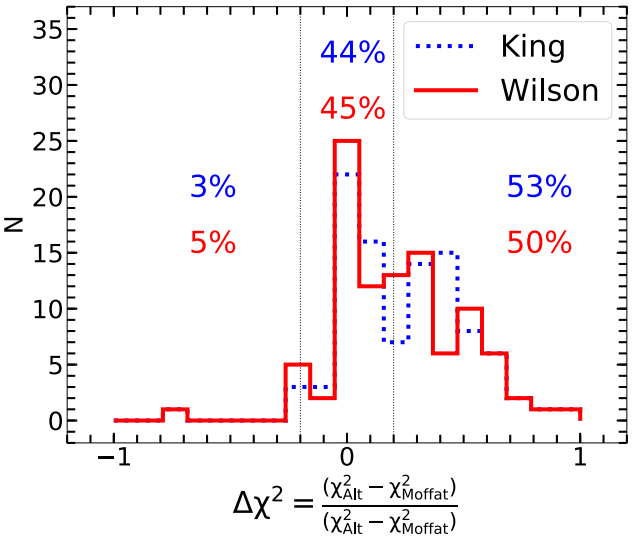

Figure 8. $\Delta\chi^2$ distributions of the Moffat-EFF selected as reference model, compared with King (blue dotted) and Wilson (red solid) models for fits in the *V* band. The reference and the comparison models are considered to be equally good for $|\Delta\chi^2| \leq 0.2$, which is signalled by the vertical dotted lines. The three columns of numbers appearing in percentage correspond to the King versus Moffat-EFF (blue) and Wilson versus Moffat-EFF (red), for $\Delta\chi^2 < -0.2$, $|\Delta\chi^2| \leq 0.2$, and $\Delta\chi^2 > 0.2$, respectively. For 44–45 per cent of the clusters, the fits are equally good for any of the three models, with Moffat-EFF model providing a better fit ($\Delta\chi^2 > 0.2$) for a further 50–53 per cent. For only 3–5 per cent of the clusters ($\Delta\chi^2 < -0.2$), King or Wilson models provide a better fit than Moffat-EFF model.

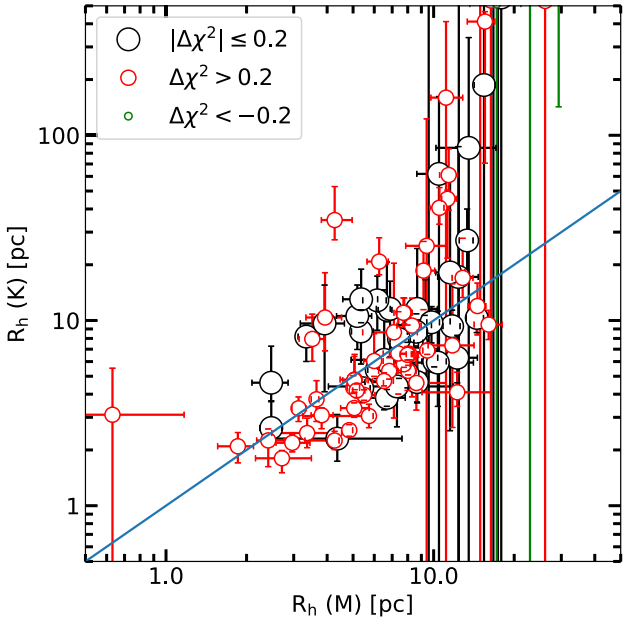

Figure 9. Half-light radius R_h of King models against those obtained from Moffat-EFF models for the 99 SSCs. Clusters are colour and size coded to indicate equally good fits with King and Moffat-EFF models (black large circles), better fit with the Moffat-EFF models (red medium-sized circles), and those well represented with the King models (green small circles). The R_h values derived from both the models agree with each other for $R_h \lesssim 10$ pc, independent of which model produced the best fit. Beyond this radius, the error bar on the R_h derived from the King models is systematically larger than those for the Moffat-EFF models. We note that this is even true for the three clusters for which the King model produced the best fit (green vertical lines).

requiring King or Wilson models. These conclusions also apply to the fits in the other two bands, but with the best-fitting Moffat-EFF percentage being around 15 per cent lower.

Thus, in general, M82 SSCs are well represented by Moffat-EFF models, and hence we will use the parameters obtained by Moffat-EFF in the *V* band as the characteristic values for all clusters. An examination of the half-light radius R_h values indicates that even for the 45 per cent of the clusters represented equally well by any one of the three models, Moffat-EFF parameters are more reliable than the other two models. In Fig. 9, we illustrate this, where we plot the R_h of King models against those obtained from Moffat-EFF models for the 99 SSCs. The error bars on R_h are obtained by propagating the errors on the basic derived parameters for each model (see Section 3.3). Clusters for which fits are equally good with King and Moffat-EFF models are distinguished from those for which Moffat-EFF models are good. It can be seen that R_h values for King models are overestimated in several cases independent of if King is a good fit or not.

In Table 3, we show the best-fitting shape (W_0 or γ), scale (r_0 or r_d), and central surface brightness (μ_0 and I_0) parameters for all the three models along with the χ^2_{min} values for the fits in the *V* band. Data for each cluster are organized in three rows: the first row shows the results for Moffat-EFF, the second row for King models, and the third row for Wilson models. For the last four columns, we give their respective error bars. The error bars on shape and scale parameters are based on the analysis in Section 3.3. The error bars in the central surface brightness are based on these errors propagated in quadrature, following the prescription of McLaughlin & van der Marel (2005). The χ^2_{min} given in Column 4 is related to the reduced χ^2_ν by the number of degrees of freedom ν, which in our case is equal to *N*pts−2 given that we have two fitted parameters. Hence, $\chi^2_\nu = \frac{\chi^2_{min}}{N\text{pts}-2}$. For all of our clusters, χ^2_ν <3 in the *V* band for at least one of the three models.

3.6 Comparison with GALFIT and ISHAPE

GALFIT (Peng et al. 2010) and ISHAPE (Larsen 1999) are two widely used tools for obtaining structural parameters of extragalactic clusters. In order to ensure that there are no systematic offsets in the values of structural parameters obtained by our fitting tool with those obtained with these two tools, we carried out the fits with the Moffat-EFF profiles on all our sample clusters with these two tools. The PSF images, as well as the fitting radius for each cluster, are retained from our analysis. In the case of ISHAPE, we oversampled our PSF image by a factor of 10 using the tool *magnify* in IRAF, as required by the code. Fittings were carried out on 2D images of 101 × 101 pixel cut-outs. Both these codes have their own algorithm for background determination. The γ values are left free for GALFIT, whereas for ISHAPE, we used our best-fitting γ values for each cluster. In Fig. 10, we compare our r_d values with those from GALFIT and ISHAPE. We observe that in general, our values are in excellent agreement with those of GALFIT, and are consistent within the errors with those of ISHAPE, but with a slope of 1.3, instead of unity. The lengths of the error bars in GALFIT are very similar to ours, whereas ISHAPE values have larger error bars. We checked that these error bars and the values do not vary much for a fixed value of $\gamma = 3$.

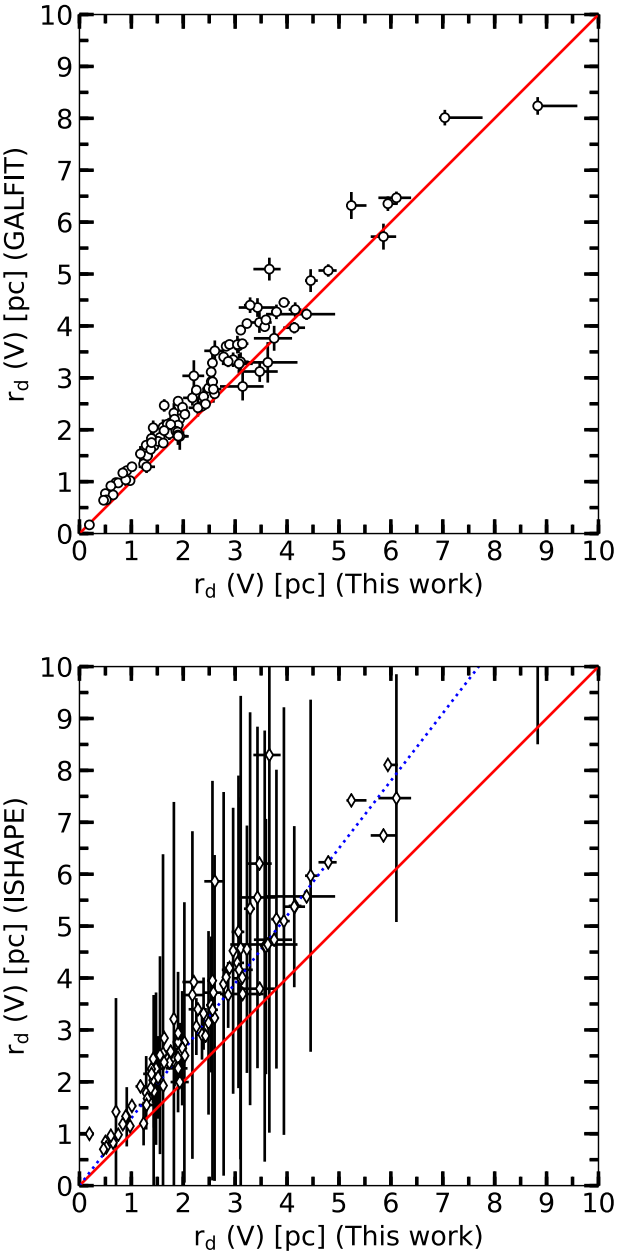

Figure 10. Comparison between Moffat-EFF r_d obtained with our own code with that obtained using GALFIT (top) and ISHAPE (bottom). The identity function is shown with a red solid line. Values from our code are in excellent agreement with that from GALFIT, whereas the ISHAPE-derived values are systematically higher by ∼30 per cent, which is indicated by a blue-dotted line of slope = 1.3.

4 RESULTS AND DISCUSSIONS

In the previous section, we concluded that Moffat-EFF models adequately represent all our subsample of 99 SSCs. Model fitting directly gives us four parameters, namely r_d, γ, μ_0, and L_{tot}. Core radius R_c, the radius at which the surface brightness is half its peak value, is related to r_d through equation (6). The half-light radius, R_h, is another parameter that can be calculated from these parameters (see Section 3.5). Dynamical analysis of the fitted model profiles, along with a knowledge of mass-to-light ratio for M82 SSCs, allows us to calculate four more parameters: mass, the central velocity dispersion σ_0, central mass density ρ_0, and central mass surface density Σ_0. Not all these parameters are independent of each other. Evolved objects like GCs show a tight inverse correlation between R_c and μ_0 (Kormendy 1985). These correlations are part of the Fundamental Plane for GCs (Djorgovski 1995; McLaughlin 2000). A detailed analysis of all the derived parameters will be carried out in a forthcoming paper. In this paper, we will characterize the basic parameters obtained in the three bands.

4.1 Colour dependence of the derived parameters

We have carried out an independent analysis of SBPs in three filters for all our sample SSCs to study the possible colour dependence of the derived parameters. In Figs 11–13, we compare the distribution of r_d, γ, and μ_0 for Moffat-EFF models in the three filters. The intention of showing these distributions is to compare the shape, as well as the centre of the distributions. Median values are indicated in all the plots by vertical dashed lines.

Median values of r_d in the three filters are very similar with a value ∼2.0 pc. In all the three filters, the distribution is asymmetric with its peak lying at ∼1 pc to the left of the median value, and having a long tail that reaches up to ∼7–9 pc. The behaviour of γ distribution is very similar to that of r_d with the median value of γ ∼ 3.0 for the three filters. μ_0 median values in the three filters are: $\mu_0(B) = 19.2$, $\mu_0(V) = 18.5$, and $\mu_0(I) = 17.5$ mag arcsec^{-2}. From these plots, we conclude that the distributions in the three filters are similar. Hence, we use the values in the V band in the rest of our analysis.

4.2 Functional form of γ distribution

Following the seminal study of Elson et al. (1987), power-law form of the SBPs represented by the Moffat-EFF profile is considered to be the characteristic feature of young SSCs. On the other hand, King profiles (King 1962) are applicable to more evolved systems such as GCs. Elson et al. (1987) found that the power-law form extends to beyond the tidal radius in young clusters. They argue that clusters take around 2–3 orbital periods to get rid of the stars outside the tidal radius, and hence, have to be older than ∼1 Gyr to show a King SBP. Until that time, the escaped stars would be located in an unbound halo.

Mackey & Gilmore (2003a) analysed the SBPs obtained from the *HST* images of a sample of 53 LMC clusters using Moffat-EFF profiles. With as much as 25 clusters in this sample being younger than ∼1 Gyr, this happens to be the only case where young and intermediate-age well-resolved clusters have been analysed using a uniform set of Moffat-EFF parameters. For this reason, the parameter set obtained by Mackey & Gilmore (2003a) has become the benchmark against which parameters of SSCs in other galaxies have been compared with. Our analysis of nearly 100 intermediate-age (50–300 Myr) SSCs offers an opportunity to understand the transition from power-law-shaped young clusters to King profile-shaped GCs.

The γ measures the slope of the power-law SBP at large radii (see equation 5). A $\gamma = 2$ corresponds to the case of a King profile with an infinite value of concentration parameter, and infinite mass. For real clusters, $\gamma > 2$. The higher the value of γ, the steeper is the outer slope. In Fig. 14 (top panel), we show the distribution of γ for M82 SSCs. The distribution is well represented by a lognormal function of $\sigma\log(\gamma) = 0.08$, centred at $\gamma = 2.88$, which is close to the median value of 3.0. This value agrees well with the median value found for clusters in the LMC and other nearby galaxies (Portegies Zwart et al. 2010). In the bottom panel, we compare the distribution of γ for

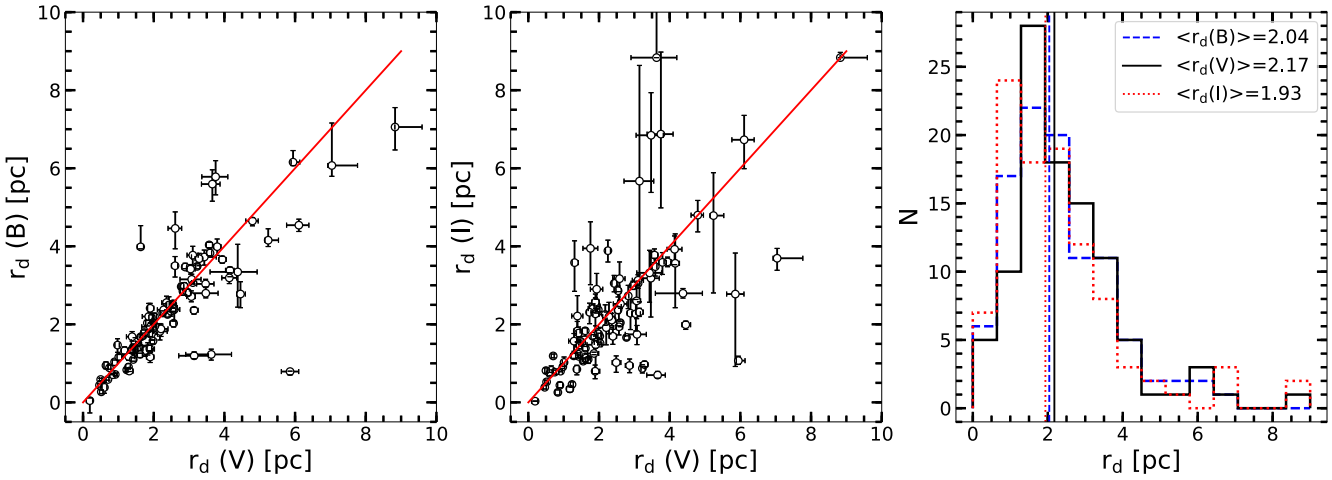

Figure 11. Comparison of $r_{\rm d}$ values obtained in three filters: $r_{\rm d}$ (B) versus $r_{\rm d}$ (V) (left), and $r_{\rm d}$ (I) versus $r_{\rm d}$ (V) (middle). The red solid line shows the identity function. Histogram of the Moffat-EFF $r_{\rm d}$ of the 99 selected clusters for the B (blue dashed line), V (black solid line), and I (red dotted line) band is shown in the right-hand panel. The median of each distribution is shown by a vertical line of the same colour code.

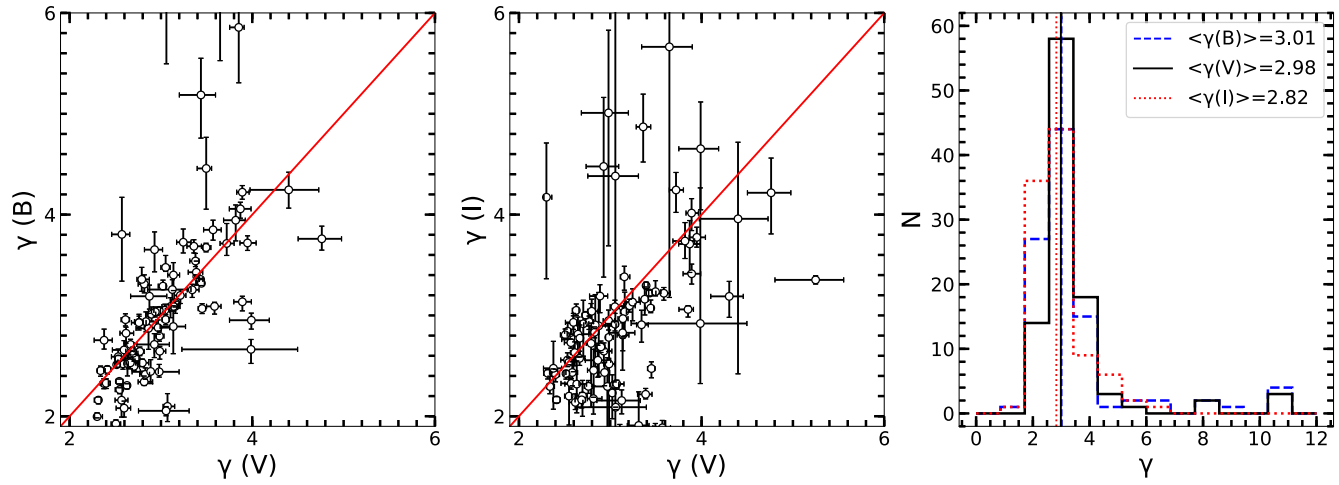

Figure 12. Comparison of γ values obtained in three filters: γ (B) versus γ (V) (left), and γ (I) versus γ (V) (middle). The red solid line shows the identity function. Histogram of the Moffat-EFF γ of the 99 selected clusters for the B (blue dashed line), V (black solid line), and I (red dotted line) band is shown in the right-hand panel. The median of each distribution is shown by a vertical line of the same colour code.

the disc clusters in M82, with those in other galaxies (LMC/SMC, M83, NGC1313, and NGC628) where measurements of γ had been carried out. Parameters for M83 come from the study of Ryon et al. (2015) and for NGC1313 and NGC628 from Ryon et al. (2017). These parameters were obtained using GALFIT. LMC/SMC cluster parameters come from the study of Mackey & Gilmore (2003a, b). We divided the sample in these galaxies into young (<50 Myr), intermediate-age (50–500 Myr), and old (>500 Myr) clusters. For the sake of comparison with M82 disc SSCs, we use the sample of intermediate-age clusters. The subsample of intermediate-age clusters includes 335 in M83, 235 in NGC628, 147 in NGC1313, and 24 in LMC/SMC.

Our distribution compares well with that in the LMC/SMC, both being lognormal centred around $\gamma = 2.9$. On the other hand, γ values distribute over a wide range in other galaxies, peaking at the minimum value of $\gamma = 2$, and decreasing almost linearly (power law) on this plot for higher values. For M83, we also show the distribution of old clusters. The sample of intermediate-age clusters of M83 shows the same behaviour as for the old sample, and hence the power-law tendency seems to be independent of evolutionary stage.

Elson et al. (1987) argued that $2.5 < \gamma < 3.2$ corresponds to density profiles in dissipationless systems. Cluster formation in their parent molecular cloud should be 100 per cent efficient for the real clusters to be dissipationless. On the other hand, real clusters are expected to contain some residual gas within the cluster volume, which would be expelled from the cluster in the first 10 Myr, when massive stars end their lives as supernovae. The loss of gravitational energy of the expelled gas mass makes the cluster expand, which eventually shapes the outer part of the density profile (Bastian & Goodwin 2006). As the residual gas fraction or equivalently efficiency of cluster formation is expected to vary from one cluster to the other, real clusters are expected to have a wide range of γ values, in this scenario of cluster formation. An alternative scenario is that the gas continues to flow into the cluster volume even after the first supernova explosions (Fujii, Saitoh & Portegies Zwart 2012; Parker et al. 2014). This is recently found to be the case in dense progenitor clouds of

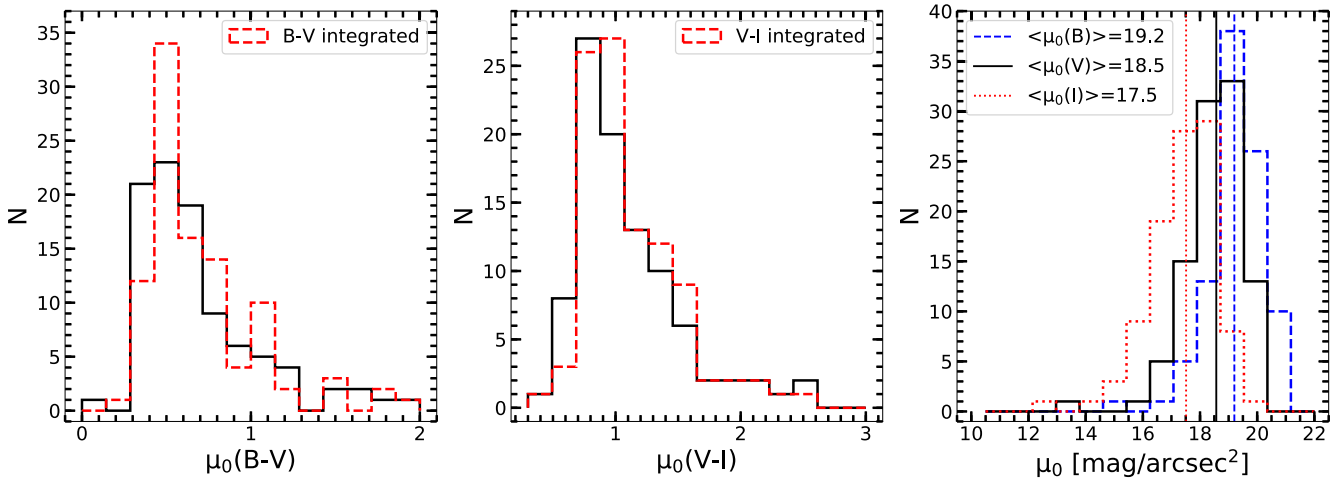

Figure 13. Central (black solid line) and integrated (red dashed line) colour histograms for $\mu_0(B) - \mu_0(V)$ (left), and $\mu_0(V) - \mu_0(I)$ (middle). Histogram of the Moffat-EFF μ_0 of the 99 selected clusters for the B (blue dashed line), V (black solid line), and I (red dotted line) band is shown in the right-hand panel. The median of each distribution is shown by a vertical line of the same colour code.

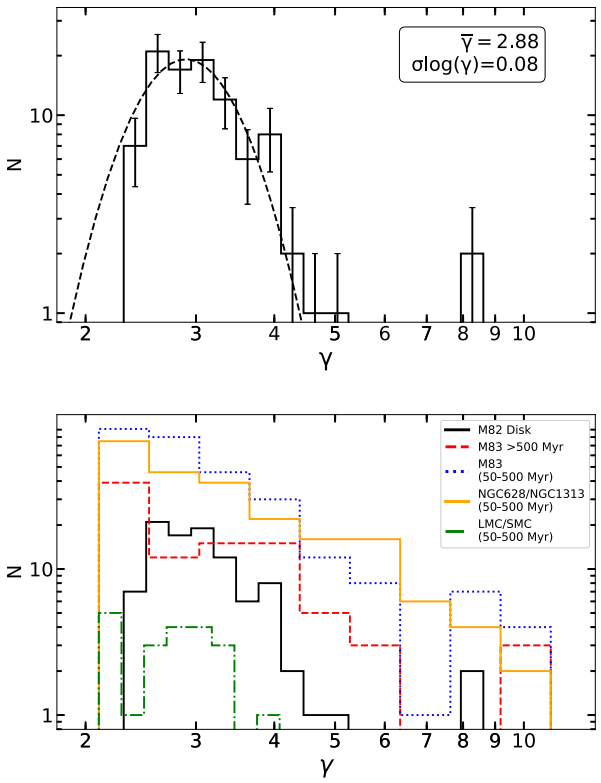

Figure 14. Upper panel: distribution of γ parameter for 99 M82 SSCs fitted with Moffat-EFF profile (histogram). The error bars are based on Poisson statistics. In dashed line, we show a lognormal fitting with a peak value of 2.88 and a standard deviation of $\sigma\log(\gamma) = 0.08$. Bottom panel: distribution of γ parameter in other nearby galaxies is compared with that of M82.

massive clusters in the Milky Way (Walker et al. 2015). Under this scenario, clusters do not necessarily expand freely following the multiple-supernovae explosions (Silich & Tenorio-Tagle 2017). It is likely that such clusters conserve their initial profile shape.

The lognormal form and the small spread in the γ value seem to support the latter scenario of cluster formation.

4.3 Functional form of R_c distribution

We now discuss the distribution of R_c for our sample of SSCs. With $R_c = 0.1$ pc (Elson et al. 1992; Mackey & Gilmore 2003a) R136 in the LMC, often considered as the prototype for a young SSC, is one of the most compact SSCs known. Several young extragalactic SSCs are also found to have sub-parsec values of R_c (Portegies Zwart et al. 2010). Bastian et al. (2008) found a tendency for R_c to increase with age, which they interpreted as an evidence for the expansion of SSCs.

In Fig. 15 (top panel), we show the distribution of the core radius R_c from our study. The distribution fits very well with a lognormal function centred at $R_c = 1.73$ pc, and $\sigma\log\left(\frac{R_c}{\rm pc}\right) = 0.25$. The median value of the distribution is 1.62 pc, which is close to the peak of the lognormal distribution. The study of Bastian et al. (2008) includes M82 disc SSCs from the spectroscopic sample of Konstantopoulos et al. (2009), for which they report a median value of $R_c = 2.2$ pc, which falls well within the range of our R_c values.

We used the same data set as for γ to compare our R_c values with that in other galaxies. In the bottom panel, we show a plot comparing the distributions, where each distribution is fitted with a lognormal function. The central value ($\overline{R_c}$) and σ of the function are given in Table 4. LMC and M83 clusters with ages similar to that in M82 disc (50–500 Myr) have mean R_c value higher and lower, respectively, as compared to that in M82. Incidentally, the morphological type of these galaxies changes from SABc in M83 (de Vaucouleurs et al. 1991), Irr II/SBd in M82 (Mayya, Carrasco & Luna 2005), to SBm in LMC (de Vaucouleurs et al. 1991). The progressive increase in mean R_c for similar-age clusters is probably suggesting that the morphological type has a role in core evolution at intermediate ages. We also note that at older (>500 Myr) ages, M83 clusters have mean R_c similar to intermediate-age clusters of M82. This tendency of R_c increasing with age in M83 has been reported by Ryon et al. (2015). Similar tendency is also seen in LMC/SMC, which has been attributed to cluster expansion by Mackey et al. (2008).

4.4 γ versus R_c relation

Dynamical evolutionary models of clusters by Mackey et al. (2008) find a steady increase of both γ and R_c with age. Different physical processes are at work at different time-scales. After the early steep

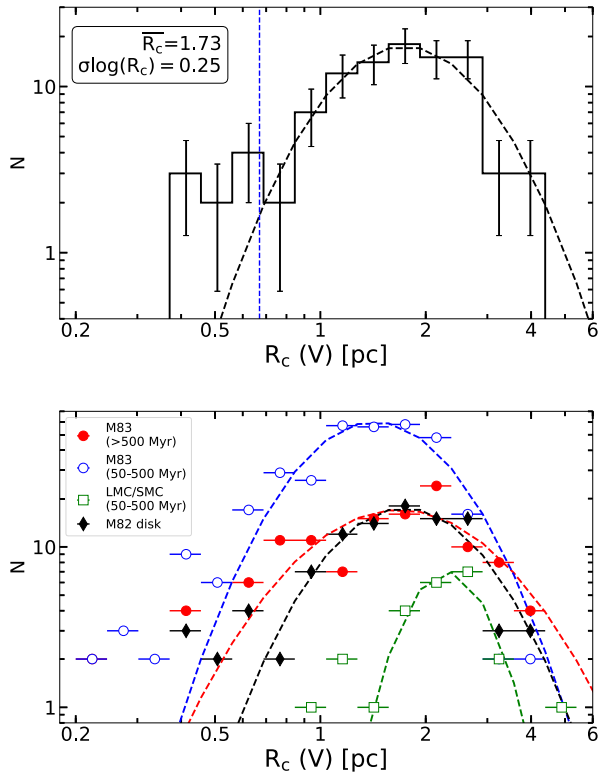

Figure 15. Upper panel: distribution of core radius R_c for 99 M82 SSCs fitted with Moffat-EFF profile (histogram). The error bars are based on Poisson statistics. In dashed line, we show a lognormal fit to the data, whose parameters are given in the top-left corner. The minimum reliable value according to the PSF is shown with a vertical blue dashed line. Bottom panel: comparison of binned distributions (symbols explained in the top-left corner) of R_c for M83 old (red), M83 intermediate-age (blue), LMC/SMC (green), and M82 (black) SSCs. The horizontal bars correspond to the fixed logarithmic width used for binning. The best-fitting lognormal function is shown by dashed lines following the same colour code as the binned data.

Table 4. Statistical properties of the Core Radius distributions in M82 and other nearby galaxies.

(1)	$\overline{R_c}$ (2)	$\sigma \log\left(\frac{R_c}{pc}\right)$ (3)	N (4)
M82 (disc)	1.73	0.25	99
M83 (50–500 Myr)	1.42	0.51	335
M83 (>500 Myr)	1.66	0.56	118
LMC/SMC (50–500 Myr)	2.29	0.39	24

Note. Col. (1): Galaxy name and age range. Col. (2): Peak value of R_c. Col. (3): Standard deviation of the lognormal distribution. Col. (4): The number of clusters in the specified age range.

increase in radius driven by residual gas expulsion, the mass-loss during stellar evolution is the principal process that drives the evolution of γ and R_c up to around 600 Myr. Such an evolution of γ and R_c is observed in the clusters in LMC and SMC (Mackey & Gilmore 2003a, b; Mackey et al. 2008).

In Fig. 16, we plot R_c against γ for our sample of SSCs (top), as well as for SMC and LMC clusters from Mackey & Gilmore (2003a,b) and M83 from Ryon et al. (2015) (bottom). For the LMC/SMC clusters, a clear trend of the upper envelope of R_c increasing with increasing γ, as expected in the models of Mackey et al. (2008), is seen. For the M82 sample, the trend is weaker.

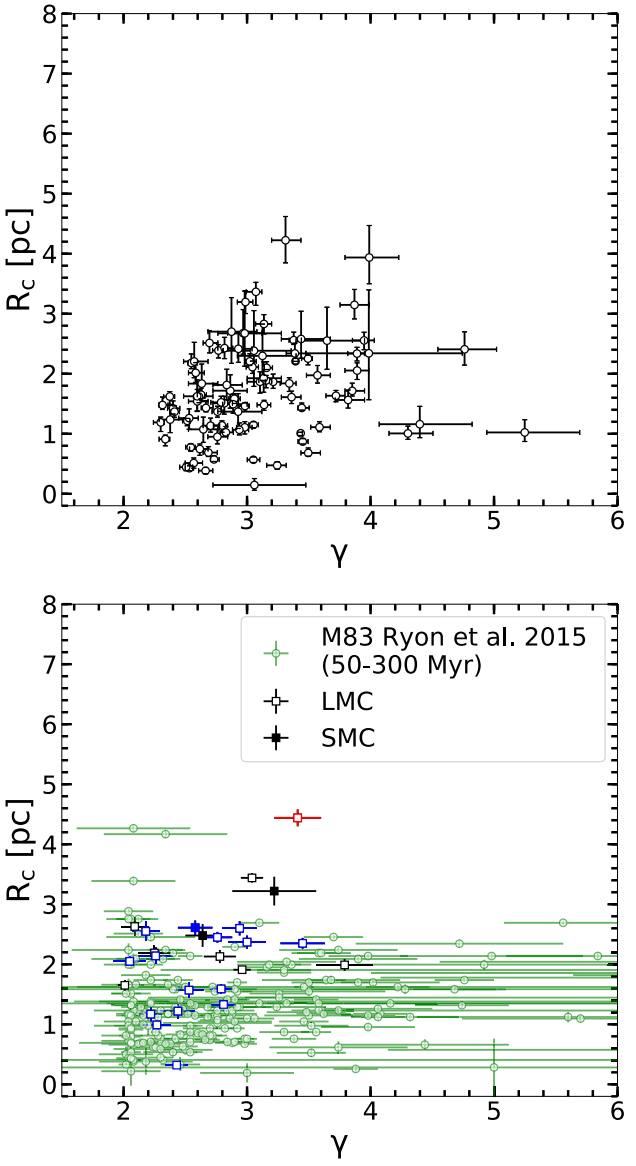

Figure 16. R_c versus γ diagram for the 99 M82 SSCs (top), and the clusters in LMC and SMC from Mackey & Gilmore (2003a,b), as well as M83 from Ryon et al. (2015) (bottom), all fitted with Moffat-EFF profiles. The bars represent the errors in the R_c versus γ plane. In both the plots, intermediate-age clusters (50–300 Myr) are shown with black symbols, and younger and older clusters are shown with blue and red symbols, respectively. The M83 data are shown in a single colour, since it only corresponds to the intermediate age range (50–300 Myr).

But the trend is also weaker for LMC/SMC and M83 SSCs that have a similar range of ages as that of M82 SSCs. Hence, the observed values of R_c and γ in M82 are in broad agreement with the predictions of Mackey et al. (2008).

5 SUMMARY

In this work, we have carried out a structural analysis of 99 intermediate-age (50–300 Myr) SSCs in the disc of M82 using the intensity profiles derived from the *HST* images in the *F435W*, *F555W*, and *F814W* bands. These clusters have a narrow range of ages between 50 and 300 Myr, which provides an excellent

opportunity to understand the structural parameters at ages intermediate between young SSCs and old GCs. Structural parameters were derived for the King, Wilson, and Moffat-EFF models, using the standard χ^2-minimization technique. Errors on the extracted parameters were determined based on the χ^2 statistics of the fitting models. Experiments on mock clusters were also carried out to authenticate the extracted parameters as well as their errors. In order to further validate our fitting technique, we obtained structural parameters with the Moffat-EFF profiles for our entire sample of clusters using widely used tools such as GALFIT and ISHAPE. We find excellent agreement with the values and their errors obtained by GALFIT, whereas ISHAPE values have systematically large errors.

The observed profiles are in general well fitted by all the three model profiles. Using quantitative criteria for discrimination between the models used, we find that the majority of clusters (∼95 per cent) are well represented by Moffat-EFF profiles. We tabulate the fitted parameters in the *F555W* band for all the clusters using the three models, and analyse in detail the statistical properties of Moffat-EFF parameters. The distributions of γ and $r_{\rm d}$ in the three bands are similar, with very similar median values. The distribution of γ follows a lognormal shape around a central value of 2.88 and $\sigma\log(\gamma) = 0.08$. The values of $\gamma < 3$ imply the existence of an extended halo in M82 clusters. The $R_{\rm c}$ distribution also follows a lognormal form with peak values of $R_{\rm c} = 1.73$ pc, and $\sigma\log\left(\frac{R_{\rm c}}{\rm pc}\right) = 0.25$. These values are large as compared to both young SSCs and old GCs, but compare well with the corresponding values for LMC intermediate-age clusters. Our γ and $R_{\rm c}$ distributions are also compared with the intermediate-age SSCs in M83, NGC1313, and NGC628. We find a larger spread of γ values in these galaxies as compared to our lognormal distribution in M82. On the other hand, $R_{\rm c}$ distributions in M83 and M82 are comparable, with systematically larger core sizes for M82 SSCs. A detailed analysis of these differences, taking into account cluster masses, ages, and host galaxy properties, will be addressed in a forthcoming paper.

ACKNOWLEDGEMENTS

We greatly appreciate the valuable suggestions we received from an anonymous referee, which has improved this manuscript, especially in the presentation of the last three figures. BCO thanks CONACYT (Consejo Nacional de Ciencia y Tecnologia) for granting PhD research fellowship that enabled her to carry out the work presented here, as well as for the research grants CB-A1-S-25070 (YDM), CB-2014–240426 (IP), and CB-A1-S-22784 (DRG), which allowed the acquisition of a cluster that was used for computations in this work. Special thanks to Sergiy Silich for accepting BCO as his research assistant during the later stages of this work.

REFERENCES

Avni Y., 1976, ApJ, 210, 642
Barmby P., McLaughlin D. E., Harris W. E., Harris G. L. H., Forbes D. A., 2007, AJ, 133, 2764
Bastian N., 2016, EAS Publ. Ser., 80, 5
Bastian N., Goodwin S. P., 2006, MNRAS, 369, L9
Bastian N., Gieles M., Goodwin S. P., Trancho G., Smith L. J., Konstantopoulos I., Efremov Y., 2008, MNRAS, 389, 223
Bastian N. et al., 2011, MNRAS, 417, L6
Baumgardt H., Hilker M., 2018, MNRAS, 478, 1520
Bertin E., 2011, in Evans I. N., Accomazzi A., Mink D. J., Rots A. H., eds, ASP Conf. Ser. Vol. 442, Astronomical Data Analysis Software and Systems XX. Astron. Soc. Pac., San Francisco, p. 435
Bertin E., Arnouts S., 1996, A&AS, 117, 393
Binney J., Tremaine S., 1987, Galactic Dynamics. Princeton Univ. Press, Princeton, NJ
Chandar R., Ford H. C., Tsvetanov Z., 2001, AJ, 122, 1330
Chandar R., Whitmore B. C., Calzetti D., Di Nino D., Kennicutt R. C., Regan M., Schinnerer E., 2011, ApJ, 727, 88
Davidge T. J., 2008, AJ, 136, 2502
de Vaucouleurs G., de Vaucouleurs A., Corwin Herold G. J., Buta R. J., Paturel G., Fouque P., 1991, Third Reference Catalogue of Bright Galaxies, Springer-Verlag, New York
Djorgovski S., 1995, ApJ, 438, L29
Elson R. A. W., Fall S. M., Freeman K. C., 1987, ApJ, 323, 54
Elson R. A. W., Schade D. J., Thomson R. C., Mackay C. D., 1992, MNRAS, 258, 103
Fall S. M., Zhang Q., 2001, ApJ, 561, 751
Forbes D. A. et al., 2018, Proc. R. Soc. London Ser. A, 474, 20170616
Freedman W. L. et al., 1994, ApJ, 427, 628
Fujii M. S., Saitoh T. R., Portegies Zwart S. F., 2012, ApJ, 753, 85
Gieles M., 2013, Mem. Soc. Astron. Ital., 84, 148
Gieles M., Zwart S. F. P., Baumgardt H., Athanassoula E., Lamers H. J. G. L. M., Sipior M., Leenaarts J., 2006, MNRAS, 804, 793
Jedrzejewski R. I., 1987, MNRAS, 226, 747
King I., 1962, AJ, 67, 471
King I. R., 1966, AJ, 71, 64
Konstantopoulos I. S., Bastian N., Smith L. J., Westmoquette M. S., Trancho G., Gallagher J. S., III, 2009, ApJ, 701, 1015
Kormendy J., 1985, ApJ, 295, 73
Larsen S. S., 1999, A&AS, 139, 393
Lynden-Bell D., Wood R., Royal A., 1968, MNRAS, 138, 495
Mackey A. D., Gilmore G. F., 2003a, MNRAS, 338, 85
Mackey A. D., Gilmore G. F., 2003b, MNRAS, 338, 120
Mackey A. D., Wilkinson M. I., Davies M. B., Gilmore G. F., 2008, MNRAS, 386, 65
McLaughlin D. E., 2000, ApJ, 539, 618
McLaughlin D. E., van der Marel R. P., 2005, ApJS, 161, 304
McLaughlin D. E., Barmby P., Harris W. E., Forbes D. A., Harris G. L. H., 2008, MNRAS, 384, 563
Mayya Y. D., Carrasco L., Luna A., 2005, ApJ, 628, L33
Mayya Y. D., Bressan A., Carrasco L., Hernandéz-Martinez L., 2006, ApJ, 649, 172
Mayya Y. D., Romano R., Rodríguez-Merino L. H., Luna A., Carrasco L., Rosa-González D., 2008, ApJ, 679, 404
Melo V. P., Muñoz-Tuñón C., Maíz-Apellániz J., Tenorio-Tagle G., 2005, ApJ, 619, 270
Moreno E., Pichardo B., Velázquez H., 2014, ApJ, 793, 110
Mutchler M. et al., 2007, PASP, 119, 1
O'Connell R. W., Gallagher John S. I., Hunter D. A., Colley W. N., 1995, ApJ, 446, L1
Parker R. J., Wright N. J., Goodwin S. P., Meyer M. R., 2014, MNRAS, 438, 620
Peng C. Y., Ho L. C., Impey C. D., Rix H.-W., 2010, AJ, 139, 2097
Portegies Zwart S. F., McMillan S. L. W., Gieles M., 2010, ARA&A, 48, 431
Press W., Teukolsky S., Vetterling W., Flannery B., 1992, Numerical Recipes in Fortran 77: The Art of Scientific Computing, 2nd edn. Cambridge Univ. Press, Cambridge
Ryon J. E. et al., 2015, MNRAS, 452, 525
Ryon J. E. et al., 2017, ApJ, 841, 92
Santiago-Cortés M., Mayya Y. D., Rosa-González D., 2010, MNRAS, 405, 1293
Silich S., Tenorio-Tagle G., 2017, MNRAS, 465, 1375
Sirianni M. et al., 2005, PASP, 117, 1049
Smith L. J., Gallagher J. S., 2001, MNRAS, 326, 1027
Sollima A., Baumgardt H., Zocchi A., Balbinot E., Gieles M., Hénault-Brunet V., Varri A. L., 2015, MNRAS, 451, 2185
Spitzer L. S., 1987, Dynamical Evolution of Globular Clusters. Princeton Univ. Press, Princeton, NJ
Walker D. L., Longmore S. N., Bastian N., Kruijssen J. M. D., Rathborne J. M., Jackson J. M., Foster J. B., Contreras Y., 2015, MNRAS, 449, 715

Wall J. V., Jenkins C. R., 2003, Practical Statistics for Astronomers. Cambridge Observing Handbooks for Research Astronomers. Cambridge Univ. Press, Leiden
Wang S., Ma J., 2013, AJ, 146, 20
Whitmore B. C., Schweizer F., 1995, AJ, 109, 960
Whitmore B. C. et al., 2016, AJ, 151, 134
Wilson C. P., 1975, AJ, 80, 175
Yun M. S., 1999, in Barnes J. E., Sanders D. B., eds, Proc. IAU Symp. 186, Galaxy Interactions at Low and High Redshift. Kluwer, Dordrecht, p. 81

SUPPORTING INFORMATION

Supplementary data are available at *MNRAS* online.
Please note: Oxford University Press is not responsible for the content or functionality of any supporting materials supplied by the authors. Any queries (other than missing material) should be directed to the corresponding author for the article.

APPENDIX A: ELLIPTICITY DISTRIBUTION OF M82 DISC SSCS

Observed structures of stellar clusters are best described by isothermal models that have intrinsically axially symmetric radial intensity profiles (e.g. King 1966). However, observed clusters are not always spherically symmetric. In such cases, it is a common practice to obtain radial intensity profiles of observed clusters using circularly symmetric isophotes. In this appendix, we discuss the effect of obtaining SBPs using almost circular isophotes for clusters that may have a non-negligible ellipticity. In Fig. A1, we show the distribution of ellipticity for our sample of 99 SSCs in the disc of M82. These ellipticities are measured at the semimajor axis $= R_{\rm fit}$ value for each cluster in the *V* band using the IRAF/STSDAS task *ellipse*. The plotted value corresponds to the average of ellipticities at three consecutive ellipses centred at $R_{\rm fit}$. In the figure, we also show the cumulative distribution of ellipticity. The distribution of ellipticities peaks at 0.19 with only 25 per cent of the SSCs having higher ellipticities. Thus, the majority of the SSCs are nearly circular.

In Fig. A2, we illustrate the effect of using almost circular rings ($\epsilon = 0.05$) for measuring the SBP of a cluster that has $\epsilon = 0.30$. We chose well-known SSC M82-F (D1), one of the most elongated clusters, for illustration. We follow the same procedure as explained in Section 3 to fit the profiles using Moffat-EFF model to the SBP obtained from $\epsilon = 0.30$. The observed SBPs obtained with $\epsilon = 0.05$ and 0.3, along with the respective best-fitting models, are shown in the figure. The $r_{\rm d}$ and γ values for these two SBPs are identical within the errors of the measurements. This illustrates that the derived structural parameters are not very sensitive to small differences in ellipticities. Hence, obtaining SBPs using circular apertures gives equally good values for clusters with ϵ as large as ∼0.3.

Table A1. Geometrical properties of M82 disc SSCs.

ID (1)	ϵ (2)	P.A. (3)
D1	0.30	56
D4	0.16	5
D7	0.41	44
D8	0.20	58
D10	0.24	53
D14	0.23	− 25
D15	0.40	71

Note. Col. (1): Numerical ID, taken from Mayya et al. (2008). Col. (2): Measured ellipticity. Col. (3): Measured position angle in degrees. The full table is shown in the electronic edition; a portion is shown here for guidance.

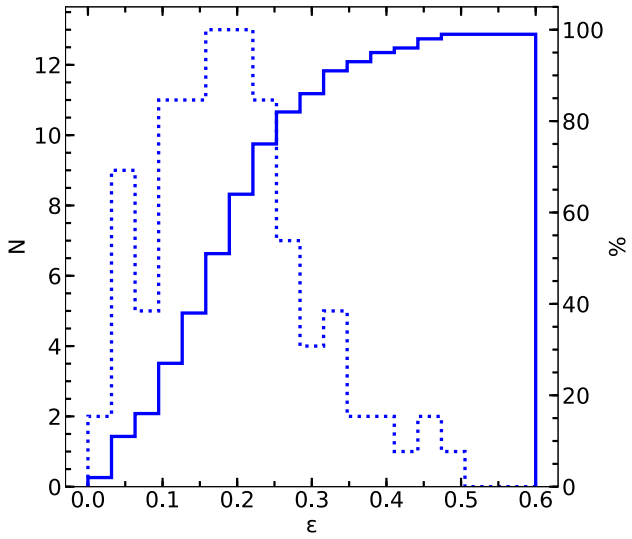

Figure A1. Distribution of ellipticities measured using elliptical isophotes of the sample of 99 M82 disc SSCs (dotted line). The cumulative distribution is shown with a solid line.

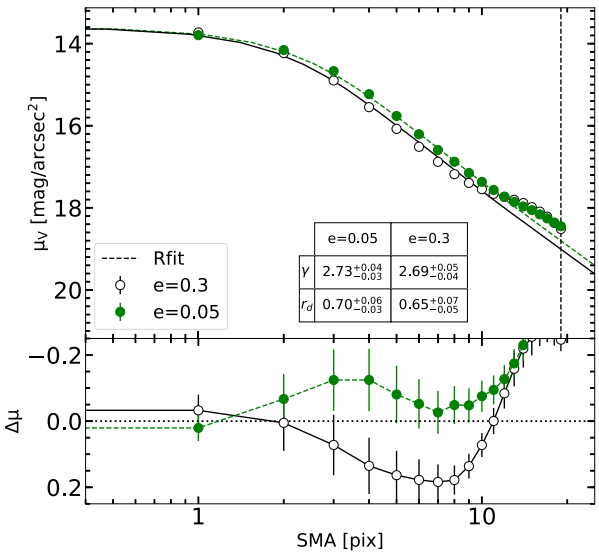

Figure A2. SBPs for the cluster D1, with nearly circular ($e = 0.05$) and with elliptical ($e = 0.3$) isophotes (upper panel) and the corresponding residuals (bottom panel).

This paper has been typeset from a TEX/LATEX file prepared by the author.